

Effects of non-adiabatic and Coriolis couplings on the bound states of He(2 3S)+He(2 3P)

D G Cocks¹, I B Whittingham¹ and G Peach²

¹ School of Engineering and Physical Sciences, James Cook University, Townsville 4811, Australia

² Department of Physics and Astronomy, University College London, London WC1E 6BT, UK

E-mail: daniel.cocks@jcu.edu.au

Abstract. The effects of non-adiabatic and Coriolis couplings on the bound states of the He(2 3S_1)+He(2 3P_j) system, where $j = 0, 1, 2$, are investigated using the recently available *ab initio* short-range $^{1,3,5}\Sigma_{g,u}^+$ and $^{1,3,5}\Pi_{g,u}$ potentials computed by Deguilhem *et al.* (*J. Phys. B: At. Mol. Opt. Phys.* **42** (2009) 015102). Three sets of calculations have been undertaken: single-channel, multichannel without Coriolis couplings and full multichannel with Coriolis couplings. We find that non-adiabatic effects are negligible for $0_u^-, 0_g^\pm, 1_u, 2_g, 2_u, 3_g$ Hund case (c) sets of levels in the $j = 2$ asymptote but can be up to 15% for some of the 0_u^+ and 1_g sets of levels where near degeneracies are present in the single-channel diagonalized potentials. Coriolis couplings are most significant for weakly bound levels, ranging from 1-5% for total angular momenta $J = 1, 2$ and up to 10% for $J = 3$. Levels near the $j = 1$ and $j = 0$ asymptotes agree closely with previous multichannel calculations based upon long-range potentials constructed from retarded resonance dipole and dispersion interactions. Assignment of theoretical levels to experimental observations using criteria based upon the short-range character of each level and their coupling to metastable ground states produces well matched assignments for the majority of observations. After a 1% increase in the slope of the $^5\Sigma_{g,u}^+$ and $^5\Pi_{g,u}$ input potentials near the classical turning point is applied, improved matching of previous assignments is obtained and further assignments can be made, reproducing very closely the number of experimental observations.

PACS numbers: 32.70.Jz, 34.50.Cx, 34.50.Rk, 34.20.Cf

Submitted to: *J. Phys. B: At. Mol. Opt. Phys.*

1. Introduction

Photoassociation (PA) of ultracold atoms provides a powerful technique for the study of the dynamics of ultracold collisions. The two interacting ultracold atoms are resonantly excited by a laser to bound states of the associated molecule with the transition energies forming a spectrum with a very high resolution of < 1 MHz, since the thermal distribution of energies in the initial scattering state is very narrow.

Photoassociation in metastable rare gases is of particular interest as the large internal energy can be released during collisions and provide experimental strategies for the study of these quantum gases. A number of experimental investigations have been conducted using PA in metastable helium as the diagnostic tool. Bound states that dissociate to the $2s^3S_1+2p^3P_2$ limit were first observed by Herschbach *et al.* [1] and more recently, Kim *et al.* [2] and van Rijnbach [3] have observed detailed structure of over 40 peaks associated with bound states with binding energies ≤ 13.57 GHz that dissociate to this limit. In addition, van Rijnbach [3] has observed six peaks lying within 0.6 GHz of the $2s^3S_1+2p^3P_1$ limit and Léonard *et al.* [4] have studied some purely long-range bound states with binding energies ≤ 1.43 GHz dissociating to the $2s^3S_1+2p^3P_0$ limit.

The bound states dissociating to the $2s^3S_1+2p^3P_0$ limit occur at interatomic separations $\geq 150 a_0$ and arise from resonance dipole and dispersion interactions that depend upon well-known atomic parameters. Theoretical analyses have been completed using both a single-channel adiabatic calculation [5] and full multichannel calculations [6] that employ long-range Born-Oppenheimer potentials constructed from retarded resonance dipole and dispersion interactions. Excellent agreement is obtained with the measured binding energies. The numerous observed peaks associated with the $2s^3S_1+2p^3P_{1,2}$ limits are not due to long-range states. Most of the peaks were identified by [7] using the accumulated phase technique for a single-channel calculation of the bound states based upon a hybrid quintet potential constructed from short-range *ab initio* $^5\Sigma_{g,u}^+$ and $^5\Pi_{g,u}^+$ potentials matched onto long-range retarded resonance dipole and dispersion potentials.

Recently Deguilhem *et al* [8] have reanalyzed the PA peaks associated with the $2s^3S_1+2p^3P_{1,2}$ limits using new fully *ab initio* multi-configuration self-consistent field (MCSCF) short-range $^{1,3}\Sigma_{g,u}^+$ and $^{1,3}\Pi_{g,u}$ potentials and multi-reference configuration interaction (MRCI) $^5\Sigma_{g,u}^+$ and $^5\Pi_{g,u}$ potentials. The body-fixed Hamiltonian in the Hund case (c) basis is diagonalized and the resulting adiabatic potentials used in a single-channel calculation, thus neglecting Coriolis and non-adiabatic couplings. Although earlier multichannel calculations for the ultra-long-range states [6] show this approximation to be quite accurate for these states, the effects of these neglected couplings on the numerous more strongly-bound shorter-range states warrants investigation. With the availability of the short-range $^{1,3,5}\Sigma_{g,u}^+$ and $^{1,3,5}\Pi_{g,u}$ potentials it is now possible to extend these multichannel calculations to the full set of bound states of the $2s^3S_1+2p^3P_{0,1,2}$ system.

We report here our results of such calculations, together with an analysis of the applicability of single-channel calculations. Atomic units are used, with lengths in Bohr radii $a_0 = 0.0529177209$ nm and energies in Hartree $E_h = \alpha^2 m_e c^2 = 27.211384$ eV.

2. Theory

2.1. Coupled-channel approach

The bound rovibrational levels of the ultracold excited metastable helium system are found by analyzing the eigenvalues of the molecular Hamiltonian

$$\hat{H} = \hat{T} + \hat{H}_{\text{rot}} + \hat{H}_{\text{el}} + \hat{H}_{\text{fs}} \quad (1)$$

where \hat{T} is the kinetic energy operator

$$\hat{T} = -\frac{\hbar^2}{2\mu R^2} \frac{\partial}{\partial R} \left(R^2 \frac{\partial}{\partial R} \right), \quad (2)$$

and \hat{H}_{rot} the rotational operator

$$\hat{H}_{\text{rot}} = \frac{\hat{l}^2}{2\mu R^2}, \quad (3)$$

for a system of two atoms $i = 1, 2$ with interatomic separation R , reduced mass μ and relative angular momentum \hat{l} . The total electronic Hamiltonian is

$$\hat{H}_{\text{el}} = \hat{H}_1 + \hat{H}_2 + \hat{H}_{12} \quad (4)$$

where the unperturbed atoms have Hamiltonians \hat{H}_i and their electrostatic interaction is specified by \hat{H}_{12} . The term \hat{H}_{fs} in equation (1) describes the fine structure of the atoms.

The multichannel equations describing the interacting atoms are obtained from the eigenvalue equation

$$\hat{H}|\Psi\rangle = E|\Psi\rangle \quad (5)$$

by expanding the eigenvector in terms of a basis of the form $|\Phi_a\rangle = |\Phi_a(R, q)\rangle$ where a denotes the set of approximate quantum numbers describing the electronic-rotational states of the molecule and q denotes the interatomic polar coordinates (θ, ϕ) and electronic coordinates $(\mathbf{r}_1, \mathbf{r}_2)$. The expansion

$$|\Psi\rangle = \sum_a \frac{1}{R} G_a(R) |\Phi_a\rangle \quad (6)$$

yields the multichannel equations

$$\sum_a \left\{ T_{a'a}^G(R) + [V_{a'a}(R) - E\delta_{a'a}] G_a(R) \right\} = 0, \quad (7)$$

where

$$T_{a'a}^G(R) = -\frac{\hbar^2}{2\mu} \langle \Phi_{a'} | \frac{\partial^2}{\partial R^2} G_a(R) | \Phi_a \rangle \quad (8)$$

and

$$V_{a'a}(R) = \langle \Phi_{a'} | [\hat{H}_{\text{rot}} + \hat{H}_{\text{el}} + \hat{H}_{\text{fs}}] | \Phi_a \rangle. \quad (9)$$

For two colliding atoms with orbital $\hat{\mathbf{L}}_i$, spin $\hat{\mathbf{S}}_i$ and total $\hat{\mathbf{j}}_i$ angular momenta, several different basis representations can be constructed. Two possibilities are the LS coupling scheme $\hat{\mathbf{L}} = \hat{\mathbf{L}}_1 + \hat{\mathbf{L}}_2$, $\hat{\mathbf{S}} = \hat{\mathbf{S}}_1 + \hat{\mathbf{S}}_2$ and $\hat{\mathbf{J}} = \hat{\mathbf{L}} + \hat{\mathbf{S}} + \hat{\mathbf{l}}$ and the jj coupling scheme $\hat{\mathbf{j}}_1 = \hat{\mathbf{L}}_1 + \hat{\mathbf{S}}_1$, $\hat{\mathbf{j}}_2 = \hat{\mathbf{L}}_2 + \hat{\mathbf{S}}_2$, $\hat{\mathbf{j}} = \hat{\mathbf{j}}_1 + \hat{\mathbf{j}}_2$ and $\hat{\mathbf{J}} = \hat{\mathbf{j}} + \hat{\mathbf{l}}$. The LS coupling scheme diagonalizes \hat{H}_{el} whereas the jj coupling scheme diagonalizes \hat{H}_{fs} . We choose to use the body-fixed jj coupled states [9]

$$|\gamma_1 \gamma_2 j_1 j_2 j \Omega_j w J m_J\rangle = \sqrt{\frac{2J+1}{4\pi}} D_{m_J \Omega_J}^{J*}(\phi, \theta, 0) |\gamma_1 \gamma_2 j_1 j_2 j \Omega_j w\rangle, \quad (10)$$

where γ_i represents other relevant quantum numbers such as $\{L_i, S_i\}$. The projections of j and J respectively onto the inter-molecular axis OZ are specified by Ω_j and $\Omega_J = \Omega_j$ which has orientation (θ, ϕ) relative to the space-fixed frame. The symmetry under inversion of the electronic wavefunction through the centre of charge is denoted by w which is equal to *gerade* (g) or *ungerade* (u). The projection of $\hat{\mathbf{J}}$ onto the space-fixed Oz axis is labelled by m_J and $D_{m_J \Omega_J}^{J*}(\phi, \theta, 0)$ is the Wigner rotation matrix [10].

The matrix elements of the various contributions to the Hamiltonian in this basis are derived in [9]. We list here the required elements using the abbreviated notation $|a\rangle = |\Phi_a(R, q)\rangle$ where $a = \{\gamma_1, \gamma_2, j_1, j_2, j, \Omega_j, w, J, m_J\}$. The radial kinetic energy terms are

$$\langle a' | \hat{T} \frac{1}{R} G_a(R) | a \rangle = -\frac{\hbar^2}{2\mu R} \frac{d^2 G_a}{dR^2} \delta_{aa'} \quad (11)$$

if we assume the R -dependence of the basis states is negligible. The rotation terms are given by

$$\begin{aligned} \langle a' | \hat{l}^2 | a \rangle = & \hbar^2 \delta_{\rho\rho'} \left\{ [J(J+1) + j(j+1) - 2\Omega_j^2] \delta_{\Omega_j' \Omega_j} \right. \\ & \left. - K_{Jj\Omega_j}^- \delta_{\Omega_j', \Omega_j-1} - K_{Jj\Omega_j}^+ \delta_{\Omega_j', \Omega_j+1} \right\}, \end{aligned} \quad (12)$$

where the quantities

$$\begin{aligned} K_{Jj\Omega_j}^\pm = & [J(J+1) - \Omega_j(\Omega_j \pm 1)]^{\frac{1}{2}} \\ & \times [j(j+1) - \Omega_j(\Omega_j \pm 1)]^{\frac{1}{2}} \end{aligned} \quad (13)$$

describe the Coriolis couplings and ρ denotes the set of quantum numbers $\{\gamma_1, \gamma_2, j_1, j_2, j, w, J, m_J\}$. The electronic terms are

$$\begin{aligned} \langle a' | \hat{H}_{\text{el}} | a \rangle = & \delta_{\eta\eta'} \sum_{LS\Omega_L\Omega_S} F_{LS\Omega_L\Omega_S}^{j_1' j_2' j' \Omega_j} \\ & \times [^{2S+1}\Lambda_w^\sigma(R) + E_a^\infty] F_{LS\Omega_L\Omega_S}^{j_1 j_2 j \Omega_j}, \end{aligned} \quad (14)$$

where the coupling coefficients $F_{LS\Omega_L\Omega_S}^{j_1 j_2 j \Omega_j}$ are given in Appendix A, $\Lambda = |\Omega_L|$, $^{2S+1}\Lambda_w^\sigma(R)$ are the Born-Oppenheimer (BO) molecular potentials for *gerade* ($w = 0$) and *ungerade* ($w = 1$) symmetries, σ is the symmetry of the electronic wave function with respect to reflection through a plane containing the internuclear axis and E_a^∞ is the

asymptotic energy of the state. The label η denotes the set of quantum numbers $\{\gamma_1, \gamma_2, \Omega_j, w, J, m_J\}$. Finally, we assume that the fine structure is independent of R so that its contribution is

$$\langle a' | \hat{H}_{\text{fs}} | a \rangle = \delta_{aa'} (\Delta E_{\gamma_1 j_1}^{\text{fs}} + \Delta E_{\gamma_2 j_2}^{\text{fs}}). \quad (15)$$

The fine structure splitting $\Delta E_{\gamma_1 j_1}^{\text{fs}}$ for the $2s^3S_1$ level vanishes and the splittings $\Delta E_{\gamma_2 j_2}^{\text{fs}}$ for the $2p^3P_0$ and $2p^3P_1$ states relative to the $2p^3P_2$ level are 31.9081 GHz and 2.2912 GHz respectively. The matrix elements of the total Hamiltonian are therefore diagonal in $\{w, J, m_J\}$.

The coupled equations (7) then become

$$\sum_a \left\{ - \left[\frac{\hbar^2}{2\mu} \frac{d^2}{dR^2} + E - \Delta E_{\gamma_2 j_2}^{\text{fs}} \right] \delta_{a'a} + \frac{\langle a' | \hat{l}^2 | a \rangle}{2\mu R^2} + \langle a' | \hat{H}_{\text{el}} | a \rangle \right\} G_a(R) = 0. \quad (16)$$

In the present investigation we seek the m_J -degenerate discrete eigenvalues $E = E_{a,v}$ and associated radial eigenfunctions $G_{a,v}(R)$, where $v = 0, 1, \dots$ labels the rovibrational levels.

In common use throughout the literature of coupled-channel calculations are the terms ‘multichannel’ and ‘close-coupled’. The term ‘close-coupled’ is often used to refer to coupled systems for which the states of interest are only strongly coupled directly to a small number of neighbouring states but may be indirectly coupled, albeit very weakly, to an endless series of states. In this situation, a limit must be imposed upon the number of states to be included in the model. In contrast, our present full multichannel calculations include all the coupled $2s2p$ states and these provide a complete basis except for the negligible couplings to other electronic states that may occur at very small interatomic distances.

2.2. Single-channel approximation

In many situations the Coriolis couplings can be neglected and the calculation of the bound states reduced to that for a single channel. This is also useful in assigning the appropriate quantum numbers to the states found by the multichannel method. The Movre-Pichler model [11], extended to include rotation, is used. At each value of R the single-channel potential is formed by diagonalizing the matrix:

$$V_{a'a}^{\Omega_j} = \langle a' | \hat{H}_{\text{el}} | a \rangle + \langle a' | \hat{H}_{\text{fs}} | a \rangle + \frac{\langle a' | \hat{l}^2 | a \rangle_{\Omega_j}}{2\mu R^2}, \quad (17)$$

where $\langle a' | \hat{l}^2 | a \rangle_{\Omega_j}$ is the part of (12) diagonal in Ω_j . The corresponding R -dependent eigenvectors are

$$|i\rangle = \sum_a C_{ai}(R) |a\rangle \quad (18)$$

and the adiabatic potential is given by $V_i^{\text{adi}}(R) = \sum_{a'a} C_{a'i}^{-1} V_{a'a}^{\Omega_j} C_{ai}$. Since we assume that the Coriolis couplings are negligible, each channel $|i\rangle$ can be labelled with the Hund’s

case (c) notation $\{J, \Omega_w^\sigma\}$ where $\Omega = |\Omega_J|$. The adiabatic eigenvalue equation for the rovibrational eigenstates $|\psi_{i,v}\rangle = R^{-1}G_{i,v}(R)|i\rangle$, where $i = \{J, \Omega_w^\sigma\}$, is then obtained by neglecting the off-diagonal elements of the kinetic energy due to non-adiabatic couplings, so that

$$\begin{aligned} \langle i' | \hat{T} \frac{1}{R} G_{i,v}(R) | i \rangle &= -\frac{\hbar^2}{2\mu R} \left(\frac{d^2 G_{i,v}}{dR^2} \delta_{ii'} \right. \\ &\quad \left. + 2 \frac{dG_{i,v}}{dR} \langle i' | \frac{d}{dR} | i \rangle + G_{i,v} \langle i' | \frac{d^2}{dR^2} | i \rangle \right). \end{aligned} \quad (19)$$

Since the term $\langle i | d|i\rangle/dR = (1/2)d\langle i|i\rangle/dR$ vanishes, the radial eigenvalue equation for the rovibrational states is

$$\left\{ -\frac{\hbar^2}{2\mu} \left[\frac{d^2}{dR^2} + U_i^{\text{KC}}(R) \right] + V_i^{\text{adi}}(R) - E_{i,v} \right\} G_{i,v}(R) = 0. \quad (20)$$

The kinetic energy correction term,

$$U_i^{\text{KC}}(R) = \langle i | \frac{d^2}{dR^2} | i \rangle = \sum_a C_{ai}(R) \frac{d^2 C_{ai}(R)}{dR^2}, \quad (21)$$

arising from the R -dependence of the diagonalized basis is small and calculable away from potential crossings but cannot be used near crossings because of discontinuities in $C_{ai}(R)$ resulting from the diabatic behaviour introduced through the use of a finite diagonalization mesh. It is not used in the present calculations.

2.3. Input potentials

The required Born-Oppenheimer potentials $^{1,3,5}\Sigma_{g,u}^+$ and $^{1,3,5}\Pi_{g,u}$ were constructed by matching the *ab initio* MCSCF and MRCI short-range potentials of [12] onto the long-range dipole-dipole plus dispersion potentials given by [6] so that

$$V_\Lambda^{\text{long}}(R) = -f_{3\Lambda}(R/\lambda)C_{3\Lambda}/R^3 - C_{6\Lambda}/R^6 - C_{8\Lambda}^\pm/R^8, \quad (22)$$

where $f_{3\Lambda}$ is an R - and Λ -dependent retardation correction [13]. The wavelength for the transition $2s^3S-2p^3P$ is λ , where $\lambda = \lambda/(2\pi) = 3258.17 a_0$. The $C_{3\Sigma}$ coefficient is $\pm 2C_3$ and $C_{3\Pi}$ is $\pm C_3$, where $C_3 = 6.41022 E_h a_0^3$. The contributions, $C_{3\Lambda}/R^3$, to the potentials are attractive (repulsive) for $S+w$ odd (even). For the van der Waals coefficients we use $C_{6\Sigma} = 2620.76 E_h a_0^6$ and $C_{6\Pi} = 1846.60 E_h a_0^6$. The $C_{8\Lambda}^\pm$ terms are $C_{8\Sigma}^+ = 1515383 E_h a_0^8$, $C_{8\Sigma}^- = 297215.9 E_h a_0^8$, $C_{8\Pi}^+ = 97244.75 E_h a_0^8$ and $C_{8\Pi}^- = 162763.8 E_h a_0^8$ [14] where the superscript indicates the sign of $(-1)^{S+w}$.

The matching of the short-range *ab initio* and long-range dipole-dipole plus dispersion potentials was undertaken at $30 a_0$ for the singlet and triplet potentials and $100 a_0$ for the quintet potentials [12]. At these matching points, R_m , the short-range potentials were shifted to agree with the long-range potentials. Although the derivatives of the short-range and long-range potentials at R_m were equal to within the accuracy of the potentials, a spline fit to the shifted tabulated short-range potentials was performed for $R \leq R_m + 3 a_0$ using the long-range potentials at the additional points

$R_m < R \leq R_m + 3a_0$ to obtain smoother matching at R_m . The analytical form (22) for the long-range potentials was used for $R > R_m + 3a_0$.

Although the short-range potentials are tabulated to within the classically forbidden region, some small variation of binding energies is possible if the $R \rightarrow 0$ extrapolation is modified. To be consistent, an extrapolation of the form $1/R + A + BR^2$ is used to emulate the expected behaviour for small interatomic distances [15]. The constants A and B are determined from the two innermost tabulated values of the potentials.

3. Numerical issues

The coupled-channel equations (16) and the single-channel equation (20) are of the form

$$\left[\mathbf{I} \frac{d^2}{dR^2} + \mathbf{Q}(R) \right] \mathbf{G}(R) = 0, \quad (23)$$

where for the case of coupled-channels, \mathbf{G} is the matrix of solutions with the second subscript labelling the linearly independent solutions. The integration region $0 \leq R \leq R_\infty$ was divided into a number of regions \mathcal{R}_α , each containing equally spaced grid points, with a step size $\Delta R_\alpha = 0.0001 a_0$ for the region closest to the origin, increasing to $0.2 a_0$ for the outermost region $R > 1000 a_0$. These equations were solved using the renormalized Numerov method [16] with the solutions for neighbouring regions matched using the values of the functions and their derivatives on the boundaries of the regions. The eigenvalues were determined by a bisection technique based on counting the nodes of the determinant $|\mathbf{G}(R)|$.

The adiabatic potentials were computed on an equally spaced diagonalization grid R_n . For a sufficiently fine grid, crossings in the coupled diabatic potentials become avoided crossings in the adiabatic potentials regardless of coupling strength. However, for weak coupling between diabatic potentials, the probability that the system follows the diabatic path is much greater than that for an adiabatic path. We choose to emulate this diabaticity by creating hybrid adiabatic/diabatic single-channel potentials. These potentials are formed by applying the function

$$Y(R_n) = \frac{2X(R_n)}{X(R_{n-1}) + X(R_{n+1})}, \quad (24)$$

where $X(R_n) = |V_a^{\text{adi}}(R_n) - V_b^{\text{adi}}(R_n)|$, to each pair of adiabatic potentials a, b . Crossings are located at points $R = R_n$ where $Y(R_n) \leq 1$ and are treated as either an avoided crossing for $Y(R_n) > \alpha$ or a true crossing for $Y(R_n) \leq \alpha$ by interchanging the potentials appropriately, where the parameter α represents the ratio of diabatic to adiabatic behaviour at the crossings. The resultant single-channel potentials $V_k^{\text{SC}}(R_n)$ possess diabatic behaviour when required, yet also allow avoided crossings to occur in some crucial regions. The single-channel basis states are then

$$|k\rangle = \sum_a D_{ak}(R_n) |a\rangle, \quad (25)$$

where D_{ak} is equivalent to C_{ai} except for interchanges of columns that correspond to the interchanges of the potentials described above. The choice of diagonalization grid size

ΔR_n significantly affects the formation of the single-channel potentials, and the values $\Delta R_n = 0.01 a_0$ and $\alpha = 0.5$ were chosen as these most closely match the multichannel results.

4. Results

4.1. Calculations

Three sets of calculations have been undertaken: (i) single-channel (SC) which ignores non-adiabatic and Coriolis couplings, (ii) multichannel without inclusion of Coriolis couplings (MC1) and (iii) full multichannel that include Coriolis couplings (MC2). The SC levels are labelled by the Hund's case (c) notation $\{J, \Omega_w^\sigma\}$, the total electronic angular momentum $j = 0, 1, 2$ of the asymptotic $2s^3S_1+2p^3P_j$ limit and to distinguish any remaining multiplicity, the minima of the potentials. The MC1 levels are labelled by $\{J, \Omega_w^\sigma\}$ and the MC2 levels by $\{J, w\}$. In this section we focus on the numerous levels that lie beneath the $j = 2$ asymptote as they are most sensitive to the short-range potentials.

4.2. Single channel

Our single-channel results for levels associated with the $2s^3S_1 + 2p^3P_2$ asymptotic limit are presented in table 1 and compared to those of [8]. Of the eight tabulated series in [8], six, including the 1_u and 2_u series presented in table 1, match very well. Almost all results are within 0.3% of the values tabulated in [8] and the maximum absolute difference is 20 MHz which is comparable to experimental accuracy. The two series that disagree are 0_u^+ , $J = 1, 3$. The differences arise from ambiguities in smoothly connecting the diagonalized potentials where the two nearly degenerate BO potentials $^{1,5}\Sigma_u^+$ cross in the region $17 a_0 < R < 17.5 a_0$ (see figure 1). Applying a fine diagonalization grid for these sets leads to avoided crossings in the single-channel potentials whereas a coarser grid gives rise to crossings. The values presented in table 1 were obtained using a fine grid of $\Delta R_n = 0.01 a_0$. We note that 1_g was the only other single-channel set that exhibited this dependence upon the diagonalization grid, due to crossings in the nearly degenerate $^{1,5}\Pi_g$ BO potentials.

4.3. Multichannel without Coriolis

Next we compare the single-channel results with those from the multichannel calculations that do not include Coriolis couplings. These methods differ only by the introduction of the non-adiabatic couplings. Although a multichannel calculation introduces new complexities into the analysis, additional benefits arise from the ability to analyze the multichannel wave functions belonging to each level.

For the majority of levels there are negligible differences between the results from the two methods. The results for the $0_u^-, 0_g^\pm, 1_u, 2_g, 2_u$ and 3_g case (c) sets agree to

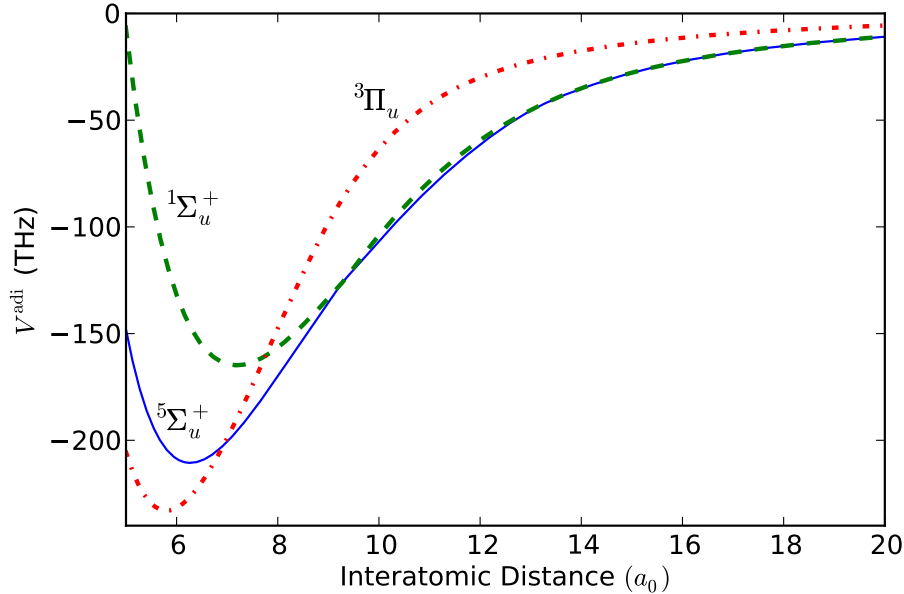


Figure 1. Single-channel potentials of the 0_u^+ , $J = 1$ manifold and their short-range case (a) assignments. The near degeneracies in the $^{1,5}\Sigma_u^+$ potentials over the region $17 a_0 < R < 17.5 a_0$ affect the determination of potential crossings in this region.

Table 1. Binding energies of the single-channel levels in units of GHz. All potentials are asymptotic to $j = 2$, were diagonalized using a grid spacing of $0.01 a_0$, and have minima of approximately -211 THz.

v	$1_u, J = 1$		$2_u, J = 2$		$0_u^+, J = 1$	
	This work	Ref [8]	This work	Ref [8]	This work	Ref [8]
70	11.319	11.301	13.666	13.647	14.583	13.658
71	7.167	7.154	9.020	9.006	9.699	9.029
72	4.316	4.307	5.703	5.692	6.205	5.735
73	2.432	2.426	3.414	3.407	3.796	3.481
74	1.250	1.246	1.913	1.908	2.215	2.015
75	0.566	0.564	0.996	0.992	1.229	1.108
76	0.216	0.215	0.478	0.476	0.642	0.572

better than 0.1% for all but the least bound levels where the differences are less than 1%. These differences are smaller than the uncertainties in the potentials and are much smaller than the uncertainties in experimental results. There are no bound levels for the 3_u set.

By contrast the 0_u^+ and 1_g case (c) sets include results that differ significantly from the single-channel results. These differences were isolated to two of the four single-channel potentials from the 0_u^+ set and three of the six single-channel potentials from the 1_g set. For the 0_u^+ sets, the differences were up to 2% for binding energies greater than 2 GHz and up to 5% otherwise. For the 1_g sets the results differed by up to 15%.

Table 2. Binding energies of the 0_u^+ , $J = 1$ and 2_u , $J = 2$ levels in the potential asymptotic to $j = 2$ in units of GHz obtained from multichannel calculations without Coriolis terms (MC1) and from single-channel calculations. The 2_u single-channel potentials labelled A and B have minima of approximately -211 THz and -233 THz respectively and the 0_u^+ single-channel potentials labelled A and B have minima of approximately -211 THz and -165 THz.

v	$2_u, J = 2$				$0_u^+, J = 1$					
	MC1	Single-Channel		Diff. (%)	v	Single-Channel			Diff. (%)	
		$j = 2$ A	$j = 2$ B			$j = 2$ A	$j = 2$ B	$j = 1$		
125	20.010	20.008		0.0	189	19.511			19.556	0.2
126	19.906		19.907	0.0	190	16.115		16.085		0.2
127	13.667	13.666		0.0	191	14.565	14.583			0.1
128	12.346		12.348	0.0	192	10.543		10.491		0.5
129	9.0227	9.0230		0.0	193	9.6694	9.6986			0.3
130	7.2495		7.2535	0.1	194	8.7252			8.7776	0.6
131	5.7068	5.7027		0.1	195	6.6048		6.5794		0.4
132	3.9174		3.9253	0.2	196	6.1999	6.2046			0.1
133	3.4205	3.4141		0.2	197	3.8897		3.9063		0.4
134	1.9247	1.9132		0.6	198	3.8223	3.7960			0.7
135	1.8065		1.8231	0.9	199	2.2539	2.2154			1.7
136	1.0050	0.9956		0.9	200	2.0855		2.1245		1.9
137	0.5395		0.5566	3.1	201	1.8130			1.8620	2.7
138	0.4824	0.4776		1.0	202	1.2618	1.2292			2.6
139	0.2113	0.2076		1.8	203	0.9663		1.0009		3.5

The levels for the remaining potentials differ by less than 0.1%. We surmise that the near degeneracies in the interacting adiabatic potentials are the cause for these differences. MC1 and SC results for the case (c) sets $2_u, J = 2$ and $0_u^+, J = 1$ are presented in table 2.

The relative proportions of each single-channel basis in the multichannel bound state eigenfunction can be calculated by applying the unitary transformation $D_{ak}(R)$ defined in equation (25). For the majority of levels only one single-channel basis state is present, indicating that there is minimal difference between the single- and multi-channel methods. Levels in the 0_u^+ and 1_g sets, however, have multiple single-channel contributions, reinforcing the observation that their binding energies differ markedly between the methods.

4.4. Multichannel with Coriolis

The final comparison we make is between the two multichannel methods, where the only difference is the inclusion or otherwise of the Coriolis couplings. Although the Coriolis couplings vary as R^{-2} and might be expected to play a significant role at small R , we do not see any difference for the more deeply bound levels. The majority of levels for the

$J = 1, 2$ ungerade sets differ between the MC1 and MC2 results by less than 0.1% and for detunings larger than 7 GHz from the $j = 2$ asymptote, all results agree to within 0.5%. These differences are slightly greater than those between the single-channel and multichannel results without Coriolis couplings. The $J = 3$ set however shows much more variance. For detunings from the $j = 2$ asymptote of more than 5000 GHz, the results differ by $< 0.5\%$ but some of the more shallowly bound levels, with detunings larger than 15 GHz, differ by up to 2%. Levels with $J > 3$ were not investigated as selection rules forbid excitation to these levels during s -wave collisions in the metastable state.

The most weakly bound levels with wavefunctions that extend from the small to large interatomic regions show the greatest effects of including Coriolis couplings. For the $J = 1, 2$ sets, approximately a third of the levels for detunings less than 7 GHz show differences ranging from 1% to 5%, which are larger than the experimental uncertainties. The $J = 3$ set shows even larger differences, with levels that can differ by up to 10% for detunings smaller than 15 GHz. These differences reflect the increase of Coriolis couplings with J and are quite significant, especially as the available experimental measurements are almost entirely within this range.

The gerade $J = 1, 2, 3$ sets have similar behaviour to the ungerade sets and show deviations up to 0.5% between the methods for detunings larger than 800, 3600 and 5000 GHz respectively. For smaller detunings, differences up to 10% do occur, although the differences for most levels remain within 0.5%. A sample comparison of the results for gerade levels obtained using multichannel calculations with and without Coriolis couplings is presented in table 3.

The differences in binding energy can be separated into two components; a shift that occurs for all levels and a splitting that occurs for degenerate MC1 $\Omega_j = \pm\Omega$ levels. The splittings between these levels in the MC2 results are generally less than 0.1% for the $J = 2$ ungerade set although several are close to 1%. For the remaining sets, the Coriolis splittings steadily increase as the detuning decreases, with most less than 2%. The greatest splittings occur when MC1 levels of different Ω manifolds are closely spaced and can be up to 10%. The only set that does not contain either the 0_u^+ or 1_g basis is the ungerade $J = 2$ set which shows the least splitting of the degenerate MC1 levels. Therefore we conclude that near degeneracies in the adiabatic potentials may be the cause for strong splitting as was observed for the differences between the SC and MC1 levels.

The contribution from each case (c) subspace for each level in the full multichannel calculation can be determined from the bound state eigenfunction. We find no obvious correlation between these case (c) proportions and the differences in the binding energies, but do observe that most levels possess large contributions from two or more case (c) sets, despite the relatively small differences in binding energies for the deeply bound states. The ungerade $J = 1, 2$ sets do possess some weakly bound levels that occupy the largest interatomic distances and these are dominated by contributions of greater than 95% from one case (c) set only.

Table 3. Binding energies of the gerade $J = 2$ set in the potential asymptotic to $j = 2$ in units of GHz obtained from multichannel calculations with (MC2) and without (MC1) Coriolis couplings. Note that levels with $\Omega > 0$ are doubly degenerate in the MC1 coupling scheme.

	MC2		MC1		Diff.(%)
	v		0_g^+	1_g 2_g	
601	4.1293		4.1474		0.4
602	4.1287		4.1474		0.5
603	3.9403			3.9174	0.6
604	3.9400			3.9174	0.6
605	3.4378			3.4205	0.5
606	3.4378			3.4205	0.5
607	3.3656		3.3889		0.7
608	3.3536		3.3889		1.0
609	2.6660	2.6552			0.4
610	2.2982		2.3116		0.6
611	2.2976		2.3116		0.6

4.5. $j = 1$ and $j = 0$ asymptotes

Calculations of energy levels near the dissociative limits $2s^3S_1 + 2p^3P_j$ for $j = 1$ and $j = 0$ introduce open channels corresponding to $j = 2$ and $j = 1, 2$ respectively into the multichannel calculation. The renormalized Numerov method is again used to find the allowed energies of the system. Due to the open channels, true bound levels appear amongst a set of artificial box states that represent the continuum of scattering states after an outer boundary wall is imposed. These artificial states are identified by examination of the wave function, or by their variability as the outer boundary is repositioned.

We find very few bound levels with purely real binding energies; too few to explain the experimental measurements. Hence, we search for any resonances that predissociate via the open channels. The search to find the complex resonance energies that smoothly match the solutions obtained by inward and outward integration [16] is performed by making use of Cauchy's argument principle, which states that a meromorphic function $f(z)$ can be shown to satisfy

$$\frac{1}{2\pi i} \oint_C \frac{f'(z)}{f(z)} dz = N - P, \quad (26)$$

where C is a bounded contour which contains N zeros and P poles. We choose the function to be the determinant $D(E) = |\mathbf{R}_m - \hat{\mathbf{R}}_{m+1}^{-1}|$ where \mathbf{R}_m and $\hat{\mathbf{R}}_{m+1}$ are ratio matrices for the outward and inward integrations respectively of the renormalized Numerov method, see equations (21) and (25) of [16]. The matching condition is then $D(E) = 0$. If $D(E)$ is assumed to be meromorphic then a region bounded by a contour should show N zeros for N valid resonances. Because poles in the same region will 'cancel' zeros then it is important to use relatively small contours such that each region

can be assumed to contain only a single zero or pole. Additionally, the matching point R_m for the function $D(E)$ must be placed so that it is within the classically permitted R region of the resonance state wave function. For resonances that extend into short interatomic distances a single value of $R_m = 100 a_0$ is sufficient to lie within the outer turning point of these resonances. Long-range resonances, however, require multiple scans at different R_m values in order to detect all resonances because the classically allowed regions of the different wave functions may not overlap. The results in this paper originated from scans using matching distances of 100, 200, 400 and 600 a_0 .

The numerical procedure uses the argument principle with a box contour that has a real width of 5 MHz, a upper imaginary boundary of 1 MHz and a lower imaginary boundary of -100 MHz. This places a limit upon the maximum predissociation that will be detected as a valid resonance. A range of real energies is scanned by using many adjacent box contours. The derivative $D'(E)$ in each integral is easily calculated numerically and the integral itself is evaluated using an adaptive Gauss-Kronrod quadrature method. This allows for a high density of grid points when required in parts of the integral and can hence handle the presence of poles and zeros in the neighbourhood of the contours.

Once regions are found that are known to contain valid resonances, the box contour of each region is narrowed using a bisection method extended to two dimensions. Because the integrals in (26) are computationally expensive to calculate, a gradient descent method is used to determine the exact resonance energy once the box edges are smaller than 1 MHz.

The single-channel results for 0_g^- near the $j = 1$ asymptote agree well with those tabulated in [8] to within 4 MHz. The full multichannel calculation for resonances that extend into the short-range region, that is, all resonances that are not purely long-range, modifies the resonance energies near the $j = 1$ asymptote by up to 5 MHz for the $J = 1$ sets, increasing to 20 MHz for the $J = 3$ sets, which is similar to the behaviour observed near the $j = 2$ asymptote. No short-range resonances are found near the $j = 0$ asymptote.

The multichannel results for the purely long-range 1_g and 0_u^+ levels near the $j = 0$ dissociation limit and the purely long-range 0_u^- and 2_u levels near the $j = 1$ dissociation limit differ by less than 1 MHz from the multichannel results of [6]. This is to be expected as these levels do not depend on the new short-range potentials. We have also examined the $1_g, J = 1$ levels in the $j = 1$ asymptote that [6] rejected as purely long-range on the grounds that barrier penetration through the double well structure of the potentials leads to significant probability for $R < 200 a_0$ and that there appeared to be appreciable predissociation. We find three pairs of resonances, $(-165.0, -164.4)$, $(-63.0, -62.7)$ and $(-16.2, -15.9)$ MHz, which do indeed possess significant short-range probability, however their predissociation widths are relatively small, ranging from 0.23 to 1.08 MHz. Each pair represents the splitting of the $\Omega_j = \pm\Omega$ degeneracy by the Coriolis couplings.

5. Experimental Assignment

5.1. Basis of assignments

Previous attempts to assign quantum numbers to experimental measurements have primarily been motivated by the desire to minimize the differences between the theoretical and experimental binding energies. In addition, knowledge of the short-range character of the individual levels is useful as this determines the likelihood of Penning ionization. Acting as both a level broadening mechanism and a detection method for most experiments, Penning ionization is extremely likely to occur if the bound level possesses singlet or triplet character in its Hund's case (a) basis for $R < 20 a_0$. We follow [17] in assuming that this probability is unity for a level with only singlet or triplet short-range character. Although single-channel calculations cannot determine accurately the short-range character of each bound level, Léonard *et al* [17] have used the absence or presence of different experimental levels to infer the rotational coupling between different case (c) subsets.

The multichannel calculations in this paper enable the complete bound state eigenfunctions to be calculated and the short-range spin- S fraction $f_{2S+1,v}$ to be determined exactly for each level, see Appendix A. To assist in assigning the experimental levels we can also calculate an approximate coupling factor \mathcal{A}_v between the excited bound state $|\Psi\rangle = \sum_a R^{-1}G_{a,v}(R)|a\rangle$ and the initial metastable ground states $R^{-1}G_g(R)|Sm_Slm_l\rangle$ where we suppress the labels $L_1 = m_{L_1} = L_2 = m_{L_2} = 0$. This factor is estimated from the Franck-Condon integral

$$\mathcal{A}_v = \frac{1}{N_g} \sum_{a,g} \langle Sm_Slm_l | \hat{H}_{\text{int}} | a \rangle \int G_g(R) G_{a,v}(R) dR, \quad (27)$$

where the matrix element of the laser interaction \hat{H}_{int} is given in Appendix B and N_g represents the number of coupled metastable states. We replace the radial eigenfunction $G_g(R)$ for the metastable state by unity, as we do not wish to specify the temperature of the system which can range from μK to mK . The Ω -degenerate levels that have been split by the Coriolis coupling form pairs, each comprised of a symmetric and an antisymmetric level. As only the symmetric level of each pair can possess a non-zero coupling, only one of the pair of Coriolis split levels can possibly be observed by experiment.

5.2. Spin-polarized experiments for $j = 2$

We first consider the experimental data of Kim *et al* [2] for spin-polarized metastable atoms in a magnetic trap at approximately $10 \mu\text{K}$. The experiment used an optical detection method and was able to measure separately the number of atoms, the optical density and the temperature of the gas after a cycle of laser pulse, thermalization and ballistic expansion. As the method is based upon thermalization, any decay path from the excited state is detected, including spontaneous emission. In the experiment, systematic scans for detunings in the range $0 - 6 \text{ GHz}$ from the $j = 2$ asymptote were performed and additional narrow scans centred upon predictions for more deeply

bound levels were carried out. Only ungerade excited levels are accessible from the spin-polarized metastable state $|22lm_l\rangle$ and higher partial waves than s -waves will contribute little to collisions at $10 \mu\text{K}$.

The theoretical calculations find a possible 118 levels with binding energies in the range $0.08 - 6 \text{ GHz}$. To identify those levels that should result in strong, narrow and experimentally detectable resonances, we impose conditions on the maximum probability of Penning ionization by insisting that the quintet short-range character be at least 87.5%, and on the minimum coupling to the metastable manifold by requiring $\mathcal{A}_v \geq 0.9 E_h$, see (27). These conditions isolate 19 levels, shown in table 4, that match almost uniquely with experimental observations. In addition, another four levels may be assigned to observations by relaxing the constraint upon one of the observability criteria; this may be justified by considering the strength of the other observability criterion. Only one experimental observation of 0.455 GHz remains unassigned. Two assignments of very close binding energies have been made to the observed level near 0.200 GHz , and the closeness of these levels may mean they are impossible to distinguish as separate in experiment. Also shown in table 4 are the case (c) contributions of greater than 20% to each level, listed in descending order of contribution.

Experimental levels above 6 GHz have not been included in the initial assignments as we would have been unable to properly determine the observability criteria without an unbroken scan region. However, the theoretical levels that are predicted to be observable in the range $6 - 14 \text{ GHz}$ have been appended to table 4, along with assignments to experimental observations if appropriate.

The theoretical levels that match have consistently lower binding energies than their assigned experimental levels. This suggests that a small correction to the input short-range potentials is required. Motivated by the observation in [18] that many ultracold molecular properties are very sensitive to the slope of the potential at the inner classical turning point and the fact that the observable levels possess strong quintet short-range character, we choose to vary the quintet MRCI potentials in this region by introducing a multiplicative factor c through the smoothing function

$$V'(R) = \begin{cases} V(R)(1 + 2c) & R < R_1 \\ V(R) [1 + c(1 + \cos a(R - R_1))] & R_1 < R < R_2 \\ V(R) & R_2 < R \end{cases} , \quad (28)$$

where $R_1 = 5 a_0$, $R_2 = 10 a_0$ and $a = \pi/(R_2 - R_1)$. The value $c = 0.005$ that represents a 1% variation which is quickly turned on through the region $5 < R < 10 a_0$, deepens the minima of the attractive ${}^5\Pi_u$ potential at $R = 5.387 a_0$ by 0.985% and moves it to a closer interatomic distance by $0.003 a_0$. The only other ungerade quintet potential ${}^5\Sigma_u^+$ is not significantly affected as it is repulsive. These varied potentials produced much better agreement with experiment and most levels are within the experimental uncertainty of 20 MHz , see table 4. A further improvement of the observability parameters for levels 0.928 and 0.228 GHz means that a relaxation of the criteria is no longer required in those cases and the observation of 0.455 GHz can be assigned to a theoretical level of

Table 4. Theoretical levels that are predicted to be experimentally observable and their assignment to the experimental data of [2]. Energies are given in GHz relative to the $j = 2$ asymptote. The third column lists the levels after a 1% variation is applied to the short-range potentials and the fourth and fifth columns are the observability quantities calculated from the results of this variation.

Exp	Theor	Variation	$\mathcal{A}_v (E_h)$	$f_{5,v}(\%)$	Case (c)	[8] assignment
-5.90	-5.729	-5.920	1.298	99.9	$2_u, J = 2$	$2_u, J = 2$
-5.64	-5.463	-5.648	1.770	97.5	$2_u, J = 3$	$0_u^+, J = 1$
-4.53	-4.394	-4.551	1.129	97.7	$1_u, 0_u^+, J = 1$	$0_u^+, J = 3$
-4.25	-4.142	-4.285	1.876	93.1	$0_u^+, 1_u, J = 3$	$1_u, J = 2$
-3.57	-3.438	-3.566	1.394	99.3	$2_u, J = 2$	$0_u^+, J = 1$
-3.37	-3.251	-3.375	2.023	98.2	$2_u, J = 3$	$2_u, J = 2$
-2.59	-2.499	-2.603	1.143	99.1	$1_u, 0_u^+, J = 1$	$1_u, J = 3$
-2.42	-2.338	-2.433	2.167	96.6	$0_u^+, 1_u, J = 3$	$1_u, J = 1$
-2.00	-1.937	-2.019	1.431	99.4	$2_u, J = 2$	$0_u^+, J = 1$
-1.88	-1.807	-1.886	2.399	99.8	$2_u, J = 3$	$2_u, J = 2$
-1.37	-1.326	-1.387	2.399	99.3	$0_u^+, 1_u, J = 1$	$1_u, J = 3$
-1.275	-1.223	-1.282	2.504	99.7	$0_u^+, 1_u, J = 3$	—
-1.22	-1.160 ^a	-1.220 ^a	0.565	100	$1_u, J = 2$	$1_u, J = 2$
-1.07	-1.013	-1.062	1.546	99.6	$2_u, J = 2$	$0_u^+, J = 1$
-0.98	-0.928 ^a	-0.973	2.957	99.2	$2_u, J = 3$	$2_u, J = 2$
-0.62	-0.589	-0.621	4.435	92.5	$0_u^+, 2_u, J = 3$	$1_u, J = 1$
-0.51	-0.487	-0.511 ^a	1.459	63.5	$2_u, J = 2$	$2_u, J = 2$
-0.455	—	-0.458	4.391	90.5	$2_u, 0_u^+, J = 3$	$0_u^+, J = 3$
-0.280	-0.263 ^a	-0.276 ^a	5.086	82.3	$0_u^+, 2_u, J = 3$	$0_u^+, J = 1$
-0.235	-0.223 ^a	-0.228	1.813	99.3	$2_u, J = 2$	$1_u, J = 1$
-0.200	-0.185	-0.199	0.993	99.9	$1_u, J = 2$	$2_u, J = 2$
—	-0.184	-0.196	3.283	93.2	$2_u, J = 3$	—
-0.185	-0.167	-0.178 ^a	4.691	86.1	$0_u^+, 1_u, J = 3$	$1_u, J = 2$
-0.09	-0.083	-0.089	2.287	99.8	$2_u, J = 2$	$0_u^+, J = 3$
-13.67	-13.259	-13.621	1.376	97.5	$2_u, J = 3$	$2_u, J = 2$
-11.70	-11.434	-11.764	1.057	96.8	$1_u, J = 1$	$1_u, J = 1$
— ^b	-9.051	-9.324	1.201	100	$2_u, J = 2$	—
-8.95	-8.705	-8.967	1.557	97.6	$2_u, J = 3$	$2_u, J = 2$
-7.45	-7.262	-7.493	1.096	97.0	$1_u, J = 1$	$1_u, J = 1$

^aObservability criteria relaxed.

^bRegion not scanned in experiment.

0.458 GHz. Unfortunately, the levels at 0.511 and 0.178 GHz require a relaxation of the criteria under the short-range variation.

The reason for the very close match between the theoretical and experimental levels resulting from the short-range variation is unclear. Variation of the non-quintet MCSCF potentials only, which are more likely to possess small inaccuracies than the MRCI quintet potentials [19], barely affects the binding energies and in some instances adversely affects the observability parameters. Variation of all the potentials however,

produces a similar improvement in the binding energies of the levels but does not allow for the assignment to the observed level at 0.455 GHz.

There is a large difference between the assignment of levels obtained from our procedure and from that of [8]. The assignment procedure of [8] rejected entire adiabatic series by characterizing the likelihood of Penning ionization of the adiabatic potentials, whereas our multichannel calculation allows us to reject levels on an individual basis. Our calculations indicate that very few levels of each series are accessible by photoassociation, implying that the logical inclination to attempt to complete an entire adiabatic series when matching to experimental measurements appears to be invalid. Interestingly, our assignments agree with those of [17] for all levels except those for which we assign two case (c) sets and those with energies of -2.42 GHz and -1.22 GHz.

5.3. Unpolarized experiments for $j = 2$

Next, we attempt to assign levels to the experimental results of van Rijnbach [3] for unpolarized metastable atoms in a magneto-optical trap at temperatures of approximately 2 mK, where detection of Penning ionization was used as the spectroscopic signal. The temperature and lack of polarization allows a large number of metastable collisional channels to contribute, and both gerade and ungerade excited states are accessible, although the dipole approximation requires that the gerade excited states can only be coupled to ungerade $l = 1$ metastable levels. The $l = 1$ centrifugal barrier is significant for these ultracold experiments as the region $R < 240 a_0$ becomes classically forbidden for colliding metastable atoms at a temperature of 1 mK.

We find a total of 345 levels with energies between -13.57 GHz and -0.045 GHz. A subset of levels is again isolated by imposing a condition upon the minimum required coupling to the metastable manifold given by $\mathcal{A}_v > 0.7 E_h$. In order to have a non-negligible Penning ionization signal for detection but to still impose an upper limit on the observable Penning ionization decay rate, we limit the quintet short-range character to $0.875 < f_{5,v} < 0.998$. The 22 levels that satisfy these conditions are shown in table 5 with their corresponding assignments.

There is reasonable agreement between the theoretical and experimental results, and again consistently smaller theoretical binding energies are observed. Applying the same short-range potential correction as in the previous section yields much improved agreement with the experimental observations and permits the inclusion of four additional assignments. One level at -0.167 GHz that was previously unassignable is now excluded. Few levels, however, are within the tight experimental uncertainties of 0.002 to 0.19 GHz. The experimental data of van Rijnbach includes 15 levels that were very weakly observed and 11 of these have not been given assignments in table 5. To do so requires a relaxation of our imposed theoretical conditions which would introduce many additional theoretical results that cannot be assigned to any experimental level. The only ‘strong’ experimental level unassigned is -2.87 GHz, although a relaxation of

the criteria is required to make an assignment to -0.52 and -0.27 GHz. The theoretical levels of -1.062 and -0.228 GHz satisfy our imposed conditions but do not correspond to any experimental level of [3]. We also note that no gerade levels are present in the assignments, although one level at a detuning of -0.109 GHz does appear in the initial calculations using the unvaried potentials. The absence of gerade levels is due not to the $l = 1$ centrifugal barrier in the metastable state as we do not specify the wave function for the metastable states in the approximate coupling factor \mathcal{A}_v but rather to the spin-conserving nature of the coupling. The $l = 1$ metastable channels are in the triplet configuration and will strongly couple to excited levels with large triplet character, levels that are very likely to undergo Penning ionization. Almost all of the 39 gerade levels with binding energies in the range 0.045 to 13.57 GHz which satisfy $\mathcal{A}_v > 0.7 E_h$ have $f_{5,v} < 0.2$. This, together with the large $l = 1$ centrifugal barrier, means that the entire gerade manifold cannot be considered for assignment to the experimental levels near the $j = 2$ asymptote.

The measurements of Tol [20] for unpolarized atoms at a temperature of 1 mK overlap for nearly all levels with the measurements of [3] listed in table 5. However, there are two additional levels, one at -0.622 GHz which fills a gap in the table corresponding to the theoretical level -0.621 GHz and the other at -0.045 GHz which can be assigned to a theoretical level with energy -0.055 GHz.

If the short-range variation is applied to all of the potentials, instead of just to the quintet MRCI potentials, similar agreement is obtained in the shift of binding energies. More importantly, however, the behaviour of the observability parameters does not change significantly, in contrast to the beneficial changes shown in table 5 arising from varying only the quintet potentials.

There is again a large difference between the assignment of levels using our procedure as opposed to that of [8]. Léonard *et al* [17] have argued that the 1_u and 2_u $J = 2$ and all the 0_u^+ assignments should not appear as they are not expected to produce ions in the adiabatic approximation. However they have made two assignments to the 2_u $J = 2$ set in the expectation that nearby overlapping levels may be the cause of these observations [21]. We do not find any nearby overlapping levels that are accessible according to our observability criteria and instead believe that the assignments must be made to the 2_u $J = 2$ set, as the multichannel calculation firmly places these levels in the ion detection regime. We conclude that the Coriolis couplings introduce a marked change in the short-range character of these states that allows ion production to occur. We find only one other level at -3.49 GHz that follows this behaviour and is assigned to 2_u $J = 2$. Our remaining assignments agree with those of [17] for all levels except those for which we assign two case (c) sets.

5.4. Unpolarized experiments ($j = 1$)

Using the method described in section 4.5 to determine appropriate bound levels and resonances, we make assignments to the experimental observations of [3] near the

Table 5. Theoretical levels predicted to be experimentally observable and their assignment to the experimental data in [3] and [20]. Energies are given in GHz relative to the $j = 2$ asymptote. The third column lists the levels after a 1% variation is applied to the short-range potentials and the fourth and fifth columns are the observability quantities calculated from the results of this variation.

Exp	Theor	Variation	$\mathcal{A}_v(E_h)$	$f_{5,v}(\%)$	Case (c)	[8] assignment
-13.57	-13.259	-13.621	0.978	97.5	$2_u, J = 3$	$2_u, J = 2$
-11.70 ^b	-11.434	-11.764	0.700	96.8	$1_u, J = 1$	$1_u, J = 1$
-11.10 ^b	-10.930	-11.224	1.042	89.5	$1_u, 0_u^+, J = 3$	$1_u, J = 2$
-8.94	-8.705	-8.966	1.107	97.6	$2_u, J = 3$	$2_u, J = 2$
-7.44	-7.262	-7.493	0.733	97.0	$1_u, J = 1$	$1_u, J = 1$
-7.01	—	-7.103	1.179	90.7	$1_u, 0_u^+, J = 3$	$1_u, J = 2$
-5.64	-5.463	-5.647	1.258	97.5	$2_u, J = 3$	$0_u^+, J = 1$
-4.53	-4.394	-4.551	0.777	97.7	$1_u, 0_u^+, J = 1$	$0_u^+, J = 3$
-4.26	-4.145	-4.285	1.333	93.1	$0_u^+, 1_u, J = 3$	$1_u, J = 2$
-3.49 ^b	-3.438	-3.566	1.214	99.3	$2_u, J = 2$	$3_g, J = 3$
-3.38	-3.251	-3.375	1.438	98.2	$2_u, J = 3$	$2_u, J = 2$
-2.87	—	—	—	—	—	$2_u, J = 4$
-2.60	-2.499	-2.603	0.850	98.9	$1_u, 0_u^+, J = 1$	$1_u, J = 3$
-2.42	-2.338	-2.433	1.541	96.6	$0_u^+, 1_u, J = 3$	$1_u, J = 1$
-2.01	-1.937	-2.019	1.246	99.4	$2_u, J = 2$	$0_u^+, J = 1$
-1.88	-1.807	-1.886	1.705	99.8	$2_u, J = 3$	$2_u, J = 2$
-1.54	-1.326	-1.387	0.986	99.3	$0_u^+, 1_u, J = 1$	$2_u, J = 4$
-1.28	-1.223	-1.282	1.780	99.7	$0_u^+, 1_u, J = 3$	$1_u, J = 1$
—	-1.013	-1.062	1.346	99.6	$2_u, J = 2$	—
-0.98	—	-0.973	2.102	99.2	$2_u, J = 3$	$2_u, J = 2$
-0.622 ^c	-0.589	-0.621	3.153	92.5	$0_u^+, 2_u, J = 3$	$1_u, J = 1$
-0.52	-0.487	-0.511 ^a	1.270	63.5	$2_u, J = 2$	$2_u, J = 2$
-0.46	—	-0.458	3.121	90.5	$2_u, 0_u^+, J = 3$	$0_u^+, J = 3$
-0.27	—	-0.276 ^a	3.616	82.3	$0_u^+, 2_u, J = 3$	$0_u^+, J = 1$
—	—	-0.228	1.578	99.3	$2_u, J = 2$	—
-0.19	-0.184	-0.196	2.334	93.2	$2_u, J = 3$	$2_u, J = 2$
—	-0.167	—	—	—	$0_u^+, 1_u, J = 3$	—
-0.08 ^b	-0.066	-0.071	2.968	99.6	$2_u, J = 3$	$0_u^+, J = 3$
-0.045 ^c	-0.050	-0.055	4.056	98.1	$0_u^+, 1_u, J = 3$	$0_u^+, J = 1$

^aObservability criteria relaxed.

^bWeakly observed.

^cMeasurement of [20] that was not observed in [3].

$He(2s^3S_1)+He(2p^3P_1)$ asymptote. Although only the closed channels are used to discard artificial resonances, the properties of the resonances in table 6 are calculated using the complete wavefunction. In addition to the observability criteria chosen previously to be $\mathcal{A}_v \gg 0.7 E_h$ and $0.90 < f_{5,v} < 0.998$, a limit to the predissociation width Γ_{pre} of 100 MHz is imposed as previously described in section 4.5. All resonances that satisfy these criteria are shown in table 6 for detunings of less than 600 MHz from the $j = 1$ asymptote. Our assignments, made by analysing contributions only from the closed channels that have asymptotes $j = 1$ and $j = 0$, agree well with those of [8].

Table 6. Theoretical levels close to the $j = 1$ asymptote and predissociation widths Γ_{pre} in MHz predicted to be experimentally observable and their assignment to the experimental data of [3]. Energies are given in GHz relative to the $j = 1$ asymptote. The third column lists the levels after a 1% variation is applied to the short-range potentials. The parameters in the fourth, fifth and sixth columns are from the resonance calculated with variation.

Exp [3]	Theor	Variation	Γ_{pre}	$\mathcal{A}_v(E_h)$	$f_{5,v}(\%)$	Case (c)	[8] assignment
-0.452	-0.427	-0.466	75.4	0.770	98.7	$0_g^-, J = 3$	$0_g^-, J = 3$
-0.343	-0.283	-0.309	7.7	1.800	98.6	$0_g^-, J = 1$	$0_g^-, J = 1$
-0.238	-0.182	-0.201	40.1	1.657	98.8	$0_g^-, J = 3$	$0_g^-, J = 3$
-0.159	-0.117	-0.128	2.3	2.082	91.1	$0_g^-, J = 1$	$0_g^-, J = 1$
-0.089	-0.065	-0.073	18.4	2.030	98.7	$0_g^-, J = 3$	$0_g^-, J = 3$
-0.043	-0.040	-0.045	1.4	2.943	99.5	$0_g^-, J = 1$	$0_g^-, J = 1$

We note that, despite our rejection of the gerade manifold for assignments near the $j = 2$ asymptote, all of these assignments near the $j = 1$ asymptote are of the gerade manifold. This may be explained by examining the adiabatic potentials and their triplet character over the entire interatomic range. If a gerade level is to be effectively coupled to the metastable manifold, it must possess triplet character at large interatomic distance yet become mostly quintet at short interatomic distance to avoid loss from ionization. The only two adiabatic potentials that are asymptotic to $j = 2$ and satisfy this requirement possess less than 10% triplet character at $300 a_0$ and must have binding energies less than 360 MHz for the classical turning point of the wave function to extend out to this region. On the other hand, the 0_g^- adiabatic potential of the $j = 1$ asymptote possesses 20% triplet character at $300 a_0$ and allows wave functions that correspond to binding energies less than 1.8 GHz to extend out to this region. Consequently, the gerade $j = 1$ levels are much more likely to be coupled to the metastable manifold without suffering significant loss from ionization.

Applying the same variation in the short-range potentials as was introduced for the $j = 2$ levels shows some improvement in agreement between the theoretical values and the measurements of [3], although it is not as large a change as might be desired.

6. Conclusions

The availability of the short-range MCSCF and MRCI potentials of [8] enabled us to undertake single-channel and multichannel calculations to study the effects of non-adiabatic and Coriolis couplings on the bound states of the $He(2s^3S_1)+He(2p^3P_j)$ system. The single-channel results agree closely with those of [8] although some discrepancies were found that result from the choice of diagonalization grid for the single-channel potentials. Inclusion of non-adiabatic couplings does not affect the binding energies very much, but the addition of Coriolis couplings does result in some significant and experimentally measurable differences in binding energies. Assignment

of theoretical levels to experimental observations, using criteria based upon the short-range character of each level and their coupling to metastable ground states, reproduces very closely the number of levels experimentally observed. The theoretical energies for $j = 2$ are consistently smaller than the experimental energies by 1.5 – 8%, but excellent agreement with experiment is obtained after a 1% increase in the slope of the input short-range quintet potentials near the inner classical turning point is applied. The same variation also produces an improved matching between the theoretical $j = 1$ values and measurements of [3]. This suggests the need for improved short-range potentials although such adjustments of even the best *ab initio* potentials are not uncommon in the theoretical calculation of physical quantities to the accuracy required in ultracold physics.

Finally we note that we have chosen to use the same C_n parameters for the potentials as in [6] and [8] rather than the more recent coefficients in [22], as we wanted to be able to make direct comparisons with results obtained in these studies. We have repeated our calculations using these new C_n values and find that the calculated binding energies differ by less than 0.1%. For the unvaried potentials there are some differences in the observability criteria and these lead to several differences in the assignments. The addition of the variation to the quintet potentials, however, produces exactly the same assignments if either set of C_n values are used.

Acknowledgments

We thank B Deguilhem for providing tabulations of the input MCSCF and MRCI potentials and A S Dickinson, J Léonard and M van Rijnbach for invaluable discussions.

Appendix A. Decomposition of excited states

In order to analyze the singlet, triplet and quintet character of the excited bound states we transform from the Hund case (c) basis $|a\rangle = |\gamma_1\gamma_2j_1j_2j\Omega_jw\rangle$ to the Hund case (a) basis $|\alpha\rangle = |\gamma_1\gamma_2LS\Omega_L\Omega_Sw\rangle$ using

$$|\gamma_1\gamma_2j_1j_2j\Omega_jw\rangle = \sum_{LS\Omega_L\Omega_S} F_{LS\Omega_L\Omega_S}^{j_1j_2j\Omega_j} |\gamma_1\gamma_2LS\Omega_L\Omega_Sw\rangle, \quad (\text{A.1})$$

where the coupling coefficients $F_{LS\Omega_L\Omega_S}^{j_1j_2j\Omega_j}$ are defined by

$$F_{LS\Omega_L\Omega_S}^{j_1j_2j\Omega_j} = [(2S+1)(2L+1)(2j_1+1)(2j_2+1)]^{\frac{1}{2}} \times C_{\Omega_L\Omega_S\Omega_j}^{LSj} \begin{Bmatrix} L_1 & L_2 & L \\ S_1 & S_2 & S \\ j_1 & j_2 & j \end{Bmatrix}. \quad (\text{A.2})$$

In (A.2), $C_{m_1m_2m}^{j_1j_2j}$ is a Clebsch-Gordan coefficient, $\begin{Bmatrix} a & b & c \\ d & e & f \\ g & h & i \end{Bmatrix}$ is the Wigner 9 – j symbol and the implicit set of quantum numbers (γ_1, γ_2) has been suppressed.

The singlet, triplet and quintet fractions of the state $G_{a,v}(R)|a\rangle$ for $R < 20 a_0$, where Penning ionization can take place, are given by

$$f_{2S+1,v} = \frac{Q_{S,v}}{\sum_{S'} Q_{S',v}}, \quad (\text{A.3})$$

where $S = 0, 1, 2$ and

$$Q_{S,v} = \sum_{L'S'\Omega'_L\Omega'_S} \delta_{SS'} \sum_a F_{L'S'\Omega'_L\Omega'_S}^{j_1 j_2 j \Omega_j} \int_0^{20 a_0} G_{a,v}(R) dR. \quad (\text{A.4})$$

Appendix B. Radiative coupling

The approximate coupling between the experimental collision channels and excited states is calculated from the matrix element between the metastable state and the excited basis states of the interaction $\hat{H}_{\text{int}} \sim \epsilon_\lambda \cdot \mathbf{d}$ for radiation of circular polarization ϵ_λ with the molecular dipole operator \mathbf{d} . The matrix element between basis states of the form (10) has been derived in [9] and is given by

$$\begin{aligned} \langle a' | \hat{H}_{\text{int}} | a \rangle &= (-1)^\lambda \sqrt{\frac{I}{\epsilon_0 c}} \sqrt{\frac{2J+1}{2J'+1}} F_{1,j,-\Omega_j,\Omega_j}^{j'_1 j'_2 j' \Omega'_j} \\ &\times \sum_b C_{\Omega_j b \Omega'_j}^{J1 J'} C_{m_j \lambda m'_j}^{J1 J'} d_{\text{at}}^{\text{sp}} \delta_{w,1-w'}, \end{aligned} \quad (\text{B.1})$$

where $\lambda = 0, \pm 1$ represents π and σ^\pm polarization respectively in the space-fixed frame, b labels the polarization components in the molecular frame, I is the laser intensity and $d_{\text{at}}^{\text{sp}}$ is the reduced matrix element of the dipole operator between the 2s and 2p atomic states. The basis states $|Sm_S l m_l\rangle$ that are relevant to experiment, of the system $\text{He}(2s^3S_1)+\text{He}(2s^3S_1)$, are obtained through the unitary transformation

$$|Sm_S l m_l\rangle = \sum_{Jm_J \Omega_j} \delta_{S,j} (-1)^{j-\Omega_j} C_{\Omega_j -\Omega_j 0}^{j J l} C_{m_S m_l m_J}^{S l J} |j_1 j_2 j \Omega_j J m_J\rangle, \quad (\text{B.2})$$

where for this case $L_1 = L_2 = 0$.

References

- [1] Herschbach N, Tol P J J, Vassen W, Hogervorst W, Woestenenk G, Thomsen J W, van der Straten P and Niehaus A 2000 *Phys. Rev. Lett.* **84** 1874–7.
- [2] Kim J, Rapol U D, Moal S, Léonard J, Walhout M and Leduc M 2004 *Eur. Phys. J. D* **31** 227–37.
- [3] van Rijnbach M 2004 Dynamical spectroscopy of transient He_2 molecules *Ph.D thesis* University of Utrecht.
- [4] Léonard J, Walhout M, Mosk A P, Müller T, Leduc M and Cohen-Tannoudji C 2003 *Phys. Rev. Lett.* **91** 073203.
- [5] Léonard J, Mosk A P, Walhout M, van der Straten P, Leduc M and Cohen-Tannoudji C 2004 *Phys. Rev. A* **69** 032702.
- [6] Venturi V, Leo P J, Tiesinga E, Williams C J and Whittingham I B 2003 *Phys. Rev. A* **68** 022706.
- [7] Dickinson A S, Gadéa F X and Leininger T 2005 *Europhys. Lett.* **70** 320–6.
- [8] Deguilhem B, Leininger T, Gadéa F X and Dickinson A S 2009 *J. Phys. B: At. Mol. Opt. Phys.* **42** 015102.
- [9] Cocks D and Whittingham I B 2009 *Phys. Rev. A* **80** 023417.

- [10] Brink D M and Satchler G R 1993 *Angular Momentum* Clarendon Press, Oxford, 3rd edition.
- [11] Movre M and Pichler G 1977 *J. Phys. B: Atom. Molec. Phys.* **10** 2631–8.
- [12] Deguilhem B 2009 (private communication).
- [13] Meath W J 1968 *J. Chem. Phys.* **48** 227–35
- [14] Marinescu M 1998 (private communication).
- [15] Bingel W A 1959 *J. Chem. Phys.* **30**, 1250–3.
- [16] Johnson B R 1978 *J. Chem. Phys.* **69** 4678–88.
- [17] Léonard J, Mosk A P, Walhout M, Leduc M, van Rijnbach M, Nehari D and van der Straten P 2005 *Eur. Phys. Lett.* **70** 190-6.
- [18] Leo P J, Venturi V, Whittingham I B and Babb J F 2001 *Phys. Rev. A* **64** 042710.
- [19] Dickinson A S 2009 (private communication).
- [20] Tol P J J 2005 Trapping and evaporative cooling of metastable helium *Ph.D thesis* Free University of Amsterdam.
- [21] Léonard J 2009 (private communication).
- [22] Zhang J-Y, Yan Z-C, Vrinceanu D, Babb J F and Sadeghpour H R 2006 *Phys. Rev. A* **73** 022710.